Simulations of Y-Junction Photonic Crystal Waveguide for Sensing Applications

Author: Roger Xavier Lera Leri.
*Facultat de Física, Universitat de Barcelona, Diagonal 645, 08028 Barcelona, Spain.**

Advisors: Elena López Aymerich and Albert Romano Rodríguez

Abstract: In this work the results of simulations of Y-Junction photonic waveguides in a 2D Photonic Crystal (PhC) based on silicon pillars are presented. The aim is to study the variation in the transmission spectra in the near-infrared (NIR) for small displacements of the pillars placed in the photonic waveguide through simulations of the electromagnetic field propagation via the Finite-Difference Time-Domain Method (FDTD). The small displacements of the pillars simulate their bends caused by stress forces of living tissues placed on their top.

I. INTRODUCTION

Since the ancient Egyptian and Mesopotamians, humanity has been searching about the optical properties of materials. Nevertheless, it has been a long path since we could understand the nature of light. In the last century, we have been developing new technologies in order to control the optical properties of materials and the propagation of light. Some up-to-date examples can be found in the revolutionary advances in telecommunication with the fiber-optic cables and photonic integrated circuits (PIC). One of the most important elements conforming these PIC systems are Photonic Crystals (PhC).

A PhC is a periodic distribution of two dielectric materials with different dielectric constants. If the dielectric constants are different enough and the absorption of light is minimal, it is possible to construct a PhC with Photonic Band Gaps (PBG) which avoids the propagation of light in a certain direction for a range of frequencies and a fixed polarization [1]. This phenomenon is analogous to the forbidden gaps in the energy band structure of a solid ionic crystal. Instead of having a periodic potential, in the PhC the periodic dielectric function, $\varepsilon(r)$, is the responsible of the PBG appearance.

The PhC that has been studied in this work is based on silicon pillars in a water medium distributed on an hexagonal lattice as can be seen in Fig. (1). Since the periodicity of the dielectric function is constraint in the xy plane, this gives raise to a 2D PhC. The height of the pillars will be about 1.5 μm. The lattice parameter (a) and the pillar's radius (r) have been fixed at 500 nm and 100 nm, respectively. These features had been previously determined by other studies and have been successfully nanofabricated [2].

Furthermore, we can introduce defects to a PhC for the purpose of trapping certain light modes within the PBG or guiding them through the PhC. An example of linear defects is a waveguide [3]. A waveguide (WG) is a modification of a linear sequence of pillars of the PhC structure. For this, some rows of pillars will be removed until the Y-Junction WG configuration is obtained. On the other hand, a point defect consists on varying a particular feature in the PhC, in this case inside the WG. Introducing these small defects in the WG, it is possible to create resonant cavities and, as a result, excite modes whose frequency lies within the PBG [4]. For this PhC, these defects will consist on adding pillars with different diameters at specific locations inside the WG.

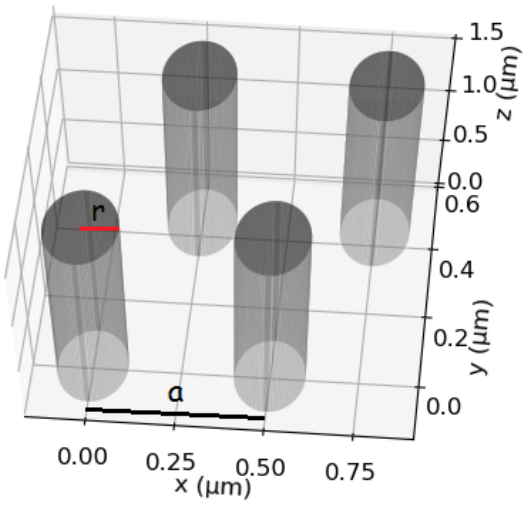

FIG. 1: Structure of the PhC. Pillars distribution in an hexagonal lattice.

In the following sections, a study of the transmission spectra for different configurations of the PhC via electromagnetic simulations using the Finite-Difference Time-Domain (FDTD) Method is presented. The main goal is to determine if it is possible to measure variations in the transmission spectra when certain pillars are displaced. A potential application of these systems will be as mechanical sensors of the stresses produced during growth and regeneration of living tissues. The idea behind the functioning of this sensor is that a tissue is fixed on the top of the pillars of the PhC. Then, its own forces will bend some pillars which will affect the transmission spectra. This is a simple way of simulating the bend of certain pillars and, hence, deduce the induced mechanical stress.

*Electronic address: rleraler22@alumnes.ub.edu

II. COMPUTATIONAL METHODS

To compute the simulation a software called MIT Electromagnetic Equation Propagation (MEEP) has been used. MEEP is an open-source software package for electromagnetic simulation via the FDTD Method [5]. This method divides the space and time into a finite grid with a certain resolution and solves the two Maxwell curl equations in derivative form in the time domain. These equations are expressed in a linearized form by means of central finite difference [6] which only considers the nearest-neighbour interaction, as the field propagation advances temporally in discrete time steps.

The main goal of the simulation is to obtain the transmission spectra of the PhC for a broadband of near-infrared (NIR) frequencies. In addition, the field pattern for a certain frequency and the dielectric distribution is also obtained as can be seen in Fig. (3).

MEEP computes a broadband response via a single computation by Fourier-transforming the response to a short pulse. To obtain the transmitted power, it computes the integral of the Poynting vector over a certain straight line (detector) in the perpendicular direction, $\hat{n}$. The detector is placed in the opposite side in relation to the PhC, to the source as shown in Fig. (2). This reads,

$$P_T(\omega) = Re\left[\hat{n} \cdot \int E_\omega(x)^* \times H_\omega(x) d^2x\right] \quad , \qquad (1)$$

where $E_\omega(x)$ and $H_\omega(x)$ are the Fourier Transforms of the electromagnetic field for every grid point in the detector:

$$F(\omega) = \frac{1}{\sqrt{2\pi}} \int e^{i\omega t} f(t) dt \approx \frac{1}{\sqrt{2\pi}} \sum_m e^{i\omega m \Delta t} f(m\Delta t) \Delta t. \qquad (2)$$

As we see in Eq. (2), $E_\omega(x)$ and $H_\omega(x)$ are calculated via summation over all discrete time steps, m, and then the transmitted power is computed. To get the transmission spectra it is necessary to normalize the transmitted power, which means that it has to be divided by the incident power. For this, it is necessary to run the simulation again, and compute the power without the PhC.

In this work, the reflection spectrum is computed as well, for which it is necessary to run the simulation twice, in the same way as for the transmission spectrum. However, the presence of an incident flux in the forward direction and a reflected flux backwards difficults its computation. It is not possible to subtract the incident power directly due to the existence of interference effects between the incident and the reflected waves. Therefore, the incident power must be obtained first. Then, the electromagnetic field with the PhC has to be computed and the electromagnetic field of the incident power, $E^0_\omega(x)$ and $H^0_\omega(x)$, has to be subtracted. This yields:

$$P_R(\omega) = Re\left[\hat{n} \cdot \int \left(E_\omega(x) - E^0_\omega(x)\right)^* \times \left(H_\omega(x) - H^0_\omega(x)\right) d^2x\right]. \qquad (3)$$

Finally, the reflected power must be normalized by the incident power.

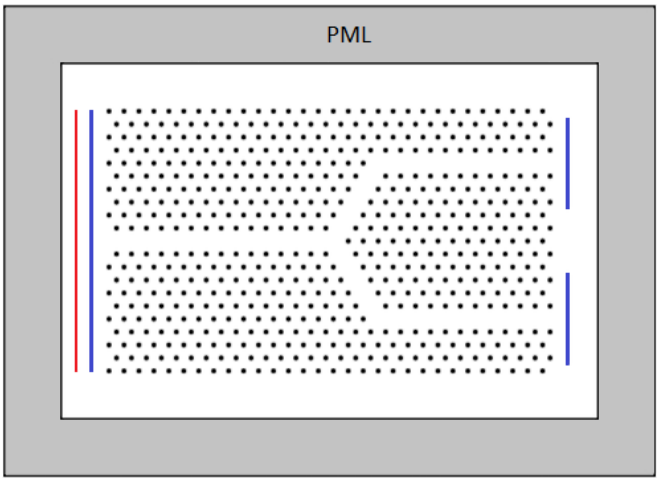

FIG. 2: Scheme of the computational cell with the PhC and the WG. The red line represents the source and blue ones are the detectors. The gray zone is the PML boundary.

III. SIMULATION

A. Cell set up and WG structure

Considering a 2D PhC in the xy plane, the computational cell has been configured to be 2D. The PhC will be placed in the center of it as shown in Fig. (2). On the left side of the PhC the source (red line) and the reflection detector (blue line) are placed. The source will consist on a Gaussian pulse transverse-magnetic (TM) polarized centered at 1.55 μm with a width large enough to obtain the complete band gap of the PhC. On the right side, two transmission detectors are placed, one for each output of the Y-Junction. Despite the fact that the source and the detectors are represented as lines in Fig. (2), they are not real objects. They just represent the regions where the integral of Poynting vector, Eq. (1) and (3), is computed.

Since we are simulating a finite system, Perfectly Matched Layers (PML) must be used. PML boundaries are a mathematical construction simulating an ideal material that absorbs all the incident waves in order to achieve a zero reflection at the edge of the computational cell.

As mentioned before, the goal of the project is to find an optimized configuration of the WG to measure significant changes in the transmission spectrum. For this, a Y-Junction WG has been designed, as shown in Fig. (2). The Y-Junction WG is supposed to allow the more precise determination of the displacements of the pillars by providing changes in two different spectra.

B. Cavities and Point Defects in the WG

In one of the branches of the WG, a cavity formed by two identical pillars separated by $2a$ will be introduced.

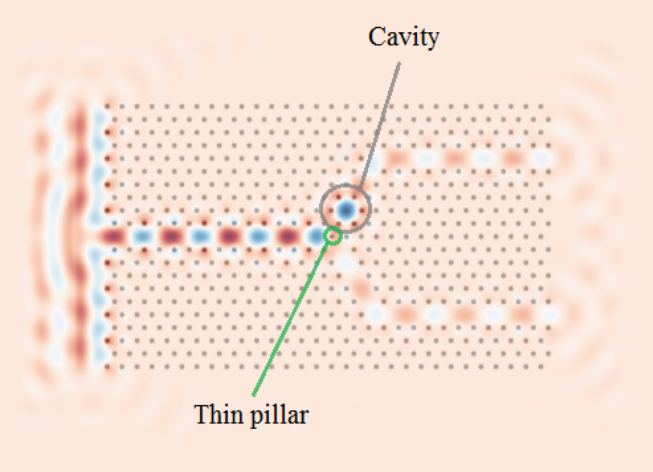

FIG. 3: First type of cavity. The plot shows the amplitude of the E_z component of the electromagnetic field for a continuous source of 1.574 μm.

This allows filtering the modes of light in the WG and achieving a peak with a high quality factor, Q, in the spectrum within the PBG. The Q-factor is defined as,

$$\mathcal{Q} = \frac{\nu_0}{\Delta\nu} \approx \frac{\lambda_0}{\Delta\lambda}, \tag{4}$$

where λ_0 is the center of peak's wavelength and $\Delta\lambda$ is the Full Width at Half Maximum (FWHM). In the bibliography high Q-factor cavities designed successfully in a pillar array based PhC are reported [7], [8].

Two different configurations have been simulated with cavities placed in the upper branch of the WG. The first one consists of a cavity created by 2 pillars of 100 nm radii separated by $2a$ and situated at the beginning of the bifurcation as is shown in Fig. (3). A pillar with a radius of 80 nm is situated at the bifurcation point, which is the one which will be displaced due to its smaller radius.

The second configuration considers a cavity centered in the diagonal part of the upper branch, as is shown in Fig. (4). The cavity is, again, constituted by 2 pillars, however, now one of them has a radius of 80 nm. Furthermore, next to each pillar there is another one forming a taper in the WG. Tapers are created in order to obtain a higher coupling efficiency in the WG [9]. Here it is used, additionally, for obtaining a sharper resonance peak. To fit this structure in the WG, the dimensions of the PhC were changed, as we can see in Fig. (4). Also, the length of the reflection detector and the source has been changed, whose length must be equal because the reflection detector also computes the incident power.

Considering that the typical stress forces in tissues are in the range of tens of nN [10], and according to the mechanical properties of the pillars, (i.e. material, radius and height) bends larger than 100 nm are not expected [11]. Therefore, for each type of cavity a set of different displacements of the thin pillar have been simulated.

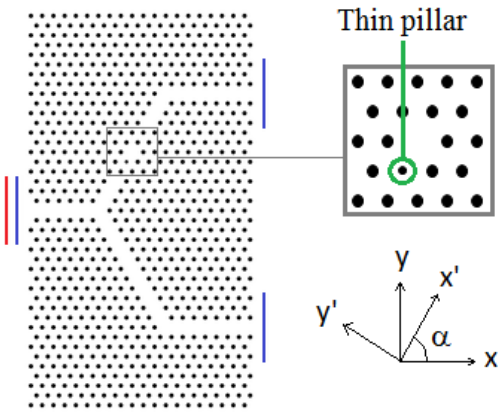

FIG. 4: Second type of cavity containing 2 pillars at each limit of the cavity. The inset is an enlargement of the region of the cavity. Coordinate system for defining the PhC (x, y) and for studying the pillar displacement (x', y'). $\alpha = 60^o$ is the rotation angle.

IV. RESULTS

First of all, we have simulated an entire PhC without a WG in order to obtain the PBG. The PBG comprehends from 1.36 to 1.87 μm. The spectra of the structure combining a PhC and a Y-Junction WG are shown in Fig. (5). It can be seen that the WG allows transmission for frequencies inside the PBG.

It must be pointed out that transmission for the upper detector is exactly the same as for the lower detector because of the symmetry of the WG. This symmetry is broken when a point defect is introduced in one of the branches, as is done in Fig. (3) and (4). Its impact is seen in Fig. (6), which represents the transmission spectra for the first type of cavity. For the upper branch, where the cavity is placed, a resonance peak appears, in

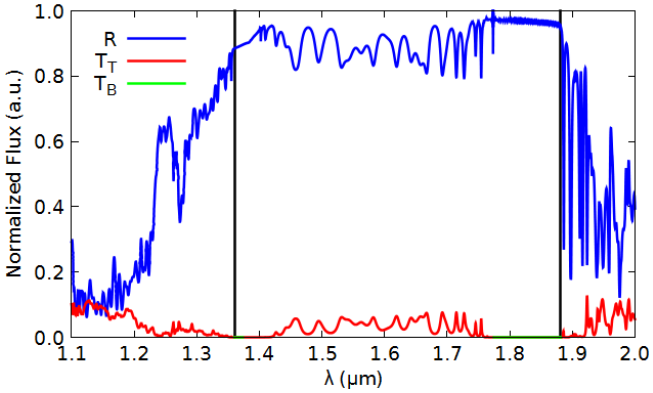

FIG. 5: Spectrum for the WG without any cavity, corresponding to the structure in Fig. (2). Vertical lines indicate the PBG region. T_T is the transmission for the top detector region and T_B is the transmission for the bottom detector region.

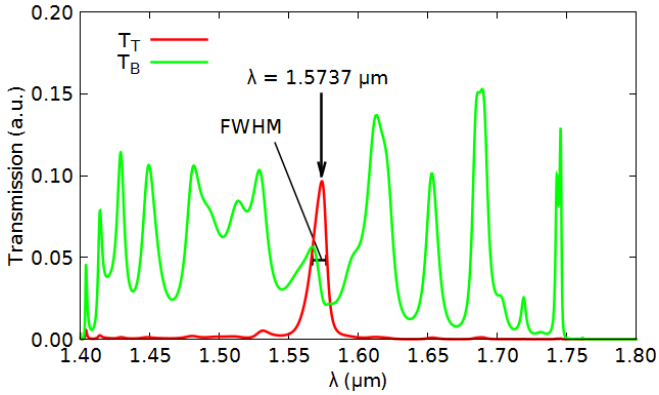

FIG. 6: Transmission for the upper and lower branch of the first cavity.

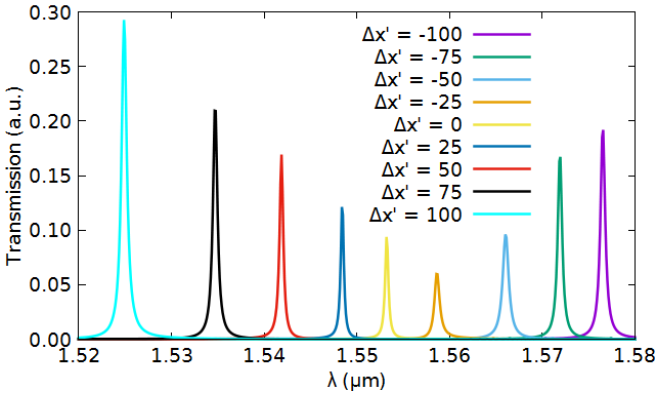

FIG. 8: Transmission spectra for the upper branch for different displacements along the x' axis of the thin pillar in the second cavity.

agreement with what is expected from the bibliography [4], [7], [8]. This peak is centered at 1.5737 μm and its amplitude is approximately 9.7%. The FWHM is about 8 nm and its Q-factor is 197. Furthermore, it can be validated from the fields distribution in Fig. (3), that at this wavelength the light is coupled in the cavity producing a resonance, and then is transmitted through the upper branch. Moreover, the transmission calculated at the lower detector also changes compared to the one in Fig. (5), due to the presence of the cavity in the upper branch.

To study the effect of the displacement of the thin pillar, this has been moved up to 100 nm from its initial position in steps of 25 nm in $\hat{x}$ and $\hat{y}$. The results are shown in Fig. (7). As can be seen, the maximum peak's shifts is about 2.3 nm. The maximum wavelength, $\lambda_{max} = 1.5757$ μm, is obtained when the displaced pillar is closest to the cavity, at 100 $\hat{x}$ + 100 $\hat{y}$ nm from the initial position, and the minimum wavelength, $\lambda_{min} = 1.5734$ μm, when it is farthest from it, at - 100 $\hat{x}$ - 100 $\hat{y}$ nm. In terms of the amplitude of the peak transmission, the smallest value, 3.8%, is obtained when the thin pillar is, as before, farthest from the cavity, and the larger amplitude, 12.0%, is obtained at , at - 25 $\hat{x}$ + 100 $\hat{y}$ nm.

Regarding the results for the second type of cavity a transmission peak in $\lambda = 1.5532$ μm with an amplitude of 9.5% has been obtained. Moreover, the FWHM is 0.7 nm and the Q-factor is 2360, approximately 12 times larger than the Q-factor of the first cavity. This result is promising for the sensing purpose, because the higher the Q-factor, the sharper the peak, and, consequently, the larger the amplitude variation at a fixed wavelength when the peak is displaced. Proceeding in a similar manner as for the first cavity, a set of displacements for the thin pillar has been simulated. In this case, the axes of the displacements have been rotated 60 degrees according to the axes scheme in Fig. (4). The reason for this rotation is to easier understand the effect of the displacement along and perpendicular to the WG.

In Fig. (8), one can see that the peak's wavelength varies almost linearly with the pillar displacement in the x' axis. In addition, the range of peak's wavelength variation is wider than in the first cavity. This result can be explained because in this case the pillar that is displaced forms the cavity, and by varying its position, logically, the dimensions of the cavity are modified. Consequently, the peak shifts occurring in the second type of cavities are larger, which is positive for the sensing application. It is shown in Fig. (8) that when the size of the cavity increases, so does the peak's wavelength. Furthermore, the Q-factor of the peaks has increased considerately in

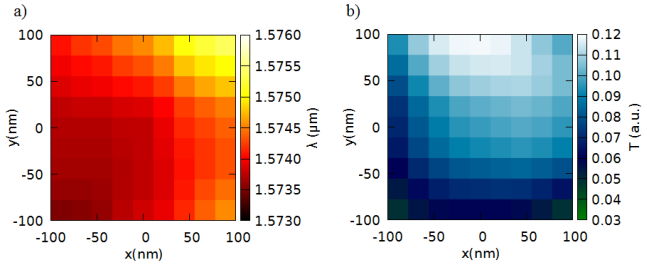

FIG. 7: Maps of values of the wavelength a) and of the amplitude b) of the transmission peaks for the different displacements of the thin pillar for the set-up in Fig. (3).

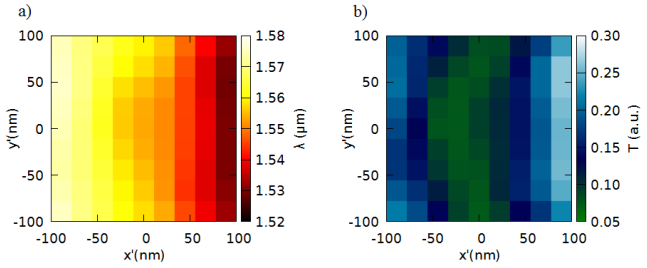

FIG. 9: Maps of values of the wavelength a) and the amplitude b) of the transmission peaks for the different displacements of the thin pillar in the set-up of Fig. (4).

relation to the peaks of the first cavity.

In Fig. (9) the maps of wavelength shift and amplitude for the second cavity for the different displacements of the thin pillar are shown. It is important to notice that the main variation is along the x' axis, while the shift is minimal and almost symmetrical when the displacement occurs along the y' axis. This is because the cavity dimension changes equally in both directions of the pillar displacement. On the one hand, the highest wavelength value, $\lambda_{max} = 1.5793$ μm corresponds to the pillar displacement of -100 $\hat{x'}$ - 100 $\hat{y'}$ nm, which gives rise to the largest cavity; on the other, the minimum wavelength value, $\lambda_{min} = 1.5248$ μm corresponds to a pillar displacement of 100 $\hat{x'}$ nm, producing the smallest cavity. The variation of the peak position now comprehends a range of 54.5 nm, nearly 24 times larger than the one observed in the first type of cavity.

The change of the amplitude of the peaks, however, is less intuitive. The maximum amplitude variation is observed along the x' axis, similar to what occurs with the peak's position. A symmetric behaviour is seen also when the displacement occurs along the y' axis.The maximum peak amplitude is 29.9%, and the minimum, 6.0%. The range is about 23.9%, nearly 3 times the one obtained with the first cavity. Thus, in terms of peak's amplitude, the second cavity is more sensitive than the first one.

V. CONCLUSIONS

Two configurations of different point defects for a Y-Junction waveguide have been simulated using the FDTD Method. In both cases, the transmission spectra have been simulated for different displacements of a narrow pillar, the defect, inside the waveguide, which simulates its bending. For the first type of cavity, formed by two pillars and a thinner pillar placed at the bifurcation point, the variation of the peak's wavelength is very limited for any displacement of the thin pillar. Despite this, the changes on amplitude of the peaks are significant.

For the second type of cavity, formed by four pillars and one of the interior pillars being the thinner one, the Q-factor of the peaks has increased significantly, as was expected, due to the taper in the waveguide. Variations in the peak's positions and amplitude have been significantly affected by displacements of the thin pillar along the waveguide direction. This is an effect of the modification of the cavity's dimensions when the pillar is displaced. Variations for displacements perpendicular to the waveguide directions are smaller because the cavity's dimension almost does not change.

To summarise, the second cavity is more sensitive to small displacements than the first one. However, it is not equally sensitive for displacements in any direction. Without taking into account fabrication and experimental issues, these results prove that for different bends of a certain reduced size pillar, variations in the transmission spectra large enough occur that should allow implementing a photonic crystal waveguide for sensing applications.

Acknowledgments

I would like to thank my two advisors, Elena and Albert, for giving me an unconditional help and encouragement to carry out this work, and also to introducing me into the research world. Moreover, I would like to thank my family for their giant support.

[1] John. D. Joannopoulos, et al. *Photonic Crystals: Molding the Flow of Light*. 2nd. ed. (Princeton University Press, 2008).

[2] López-Aymerich, E.. "Design, fabrication and characterisation of Si nanopillars-based photonic crystal for mechanical sensing". *Dipòsit Digital UB*, 2018.

[3] Wilson, R. et al. "Efficient photonic crystal Y-Juction". *J. Opt. A: Pure Appl. Opt.*, vol. 5, pp. 76-80, 2003.

[4] Villeneuve, P. R. et al. "Microcavities in photonic crystals: Mode symmetry, tunability, and coupling efficiency". *Phys. Rev. B.*, vol. 54, pp. 7837-7842, 1996.

[5] *https://meep.readthedocs.io/en/latest/* (Last visited: 14/06/2020)

[6] Karl S. Kunz and Raymond J. Luebbers. *The Finite Difference Time Domain Method for Electromagnetics*. 1st. ed. (CRC PRESS, Florida, 1993).

[7] Xu, T. et al. "Pillar-array based optical sensor". *Opt. Express*, vol. 18, pp. 5420-5425, 2010.

[8] Xu, T. et al. "A pillar-array based two-dimensional photonic crystal microcavity". *Appl. Phys. Lett.*, vol. 94, pp. 241110, 2009.

[9] Sanchis, P. et al., "Experimental demonstration of high coupling efficiency between wide ridge waveguides and single-mode photonic Crystal waveguides". *IEEE Phot. Tech. Lett.*, vol. 16, pp. 2272-2274, 2004.

[10] Li, B. et al. "Application of sensing techniques to cellular force measurement". *Sensors (Basel)*, vol. 10, pp. 9948-9962, 2010.

[11] Rodriguez Garcia, I. "Nanopillar structures for stress measurements in biological tissues". Unpublished, 2016.